Equivalent Circuit Model Separating Dissipative and Radiative Losses for the Systematic Design of Efficient Microstrip-Based On-Chip Antennas

Benedikt Sievert, *Member, IEEE*, Jan Taro Svejda, *Member, IEEE*, Jonathan Wittemeier, Nils Pohl, *Senior Member, IEEE*, Daniel Erni, *Member, IEEE*, and Andreas Rennings, *Member, IEEE*

***Abstract*— This article presents a comprehensive method to efficiently design capacitively enhanced resonant on-chip antennas using an equivalent circuit (EC) model instead of computationally demanding full-wave simulations. To systemize the design process by predicting the radiation efficiency, the input impedance, the current and voltage distributions, and the radiation pattern of the antenna based on an EC, a method to extract both dissipation and radiation mechanisms from full-wave simulation data is described and carried out. Based on this separation of loss mechanisms, an EC-based antenna optimization with respect to the radiation efficiency is conceivably possible. Additional to the EC, which enables this efficient antenna optimization and increases the physical insight in the radiation mechanism, an analytical estimation of key antenna parameters, as the resonant length, is presented. The results from the analytical calculations and the antenna parameters calculated using the EC model are compared with full-wave FDTD simulations and used to discuss the capabilities and limitations of the EC model. Finally, an on-chip antenna of the considered type operating at 290–300 GHz and manufactured with silicon–germanium technology is used to verify the full-wave antenna simulations and the presented approach in general.**

***Index Terms*— Antennas' theory and design, equivalent circuit (EC), millimeter-wave and terahertz components, passive component modeling, silicon–germanium (SiGe/Si) technologies.**

I. Introduction

THE need for highly efficient mm-wave on-chip antennas manifests in numerous applications, namely high-resolution radar imaging [1], detailed material characterization [2], and high-data-rate communication [3]. A key parameter to increase the performance of the overall system is reducing the loss contributions of the transducer between the front end and free space, namely the antenna. These loss contributions include the impedance mismatch between the front end and antenna, the radiation efficiency of the antenna itself, and the spatial distribution of the radiated power, namely the directivity. A desirable antenna design process considers all the mentioned parameters and seeks for a (local) optimum given the desired operation frequency, bandwidth, and antenna gain with the constraint of a limited available chip area. Here, we will introduce an equivalent circuit (EC) model for a resonant microstrip antenna enhanced with series capacitances to increase its radiation efficiency in the on-chip environment. The on-chip environment usually inherits a very small distance between the uppermost and lowermost metal layers, resulting in a limited radiation efficiency of frontside radiating on-chip antennas utilizing an on-chip ground plane [4] and, thus, a reduced gain [5], [6]. To solve this issue, the use of series capacitances increasing the fringing fields and, thus, the radiation efficiency has been shown to be a promising measure [7]. Alternative approaches increase the distance between the antenna and the ground by an off-chip ground [8], which can be extended to a closed air cavity [9]. These approaches can even achieve a moderate bandwidth by the use of fractal antennas [10] or multiband reception by combining antennas [11]. By use of dielectric resonators [12]–[14] or high-dielectric superstrates [15], the outcoupling efficiency can be increased, where at least the first ones are strongly dependent on proper alignment techniques [16]. At the cost of further fabrication effort, nonplanar antenna approaches can achieve a drastically increased efficiency [17] and even high gain [18]. Opposing to the here considered frontside radiating on-chip antenna techniques, backside radiation through the semiconductor substrate and off-chip antennas [19] are also possible. Further details about the frontside and backside radiating antennas and the corresponding antenna properties can be found in [20].

The EC model presented here aims to increase the physical insight into the radiation mechanisms of microstrip-based antennas and enable a fast optimization and design process. It allows not only for the simplified description of complex, electrodynamic radiation mechanisms by an EC but also for the identification of radiating structures and their contribution to the antenna's performance. The thorough extraction and separation of radiation and dissipation losses from full-wave simulations into EC models and the resulting prediction of

Manuscript received July 29, 2020; revised October 2, 2020; accepted October 29, 2020. Date of publication December 24, 2020; date of current version February 4, 2021. This work was supported by the Deutsche Forschungsgemeinschaft (DFG, German Research Foundation) under Project 287022738—TRR 196 MARIE. *(Corresponding author: Benedikt Sievert.)*

Benedikt Sievert, Jan Taro Svejda, Daniel Erni, and Andreas Rennings are with the Center for Nanointegration Duisburg-Essen (CENIDE), Department of General and Theoretical Electrical Engineering (ATE), University of Duisburg-Essen, 47048 Duisburg, Germany (e-mail: benedikt.sievert@uni-due.de).

Jonathan Wittemeier and Nils Pohl are with the Institute of Integrated Systems, Ruhr University Bochum, 44801 Duisburg, Germany.

Color versions of one or more figures in this article are available at https://doi.org/10.1109/TMTT.2020.3040453.

Digital Object Identifier 10.1109/TMTT.2020.3040453

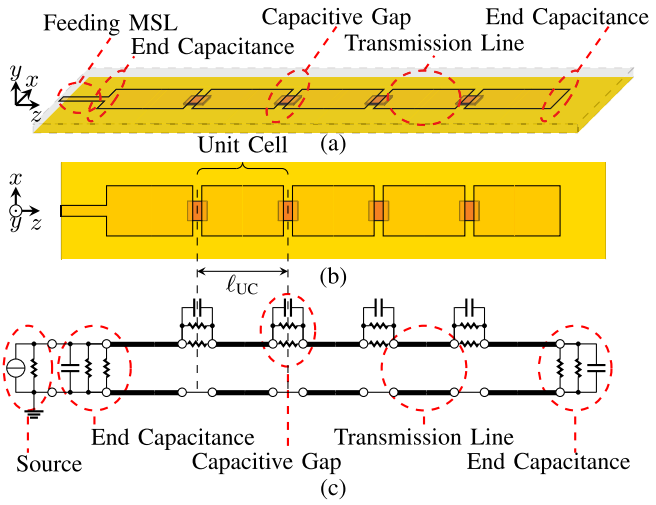

Fig. 1. Realization example of a capacitively enhanced antenna utilizing four capacitive gaps and a single-ended microstrip feedline. (a) Perspective view. (b) Top view. (c) EC model assuming a zero-length feeding microstrip line (MSL).

input impedance, radiation efficiency, and directivity derived from circuit simulations are novel to the best of our knowledge.

This article is organized as follows. Section II will introduce the generic antenna design and a corresponding EC model assembled out of building blocks. Based on the EC model, Section III presents an analytical way to estimate the necessary total antenna length and the approximate radiation efficiency. To define the parameters of the EC elements, Section IV provides and utilizes a method to extract the frequency-dependent parameters based on full-wave simulations. Section V uses an antenna design based on the analytical calculation to compare key antenna parameters predicted by the EC model to the outcome of a full-wave finite-difference time-domain (FDTD) simulation. Finally, in Section VI, the gain of an on-chip antenna based on the presented method will be measured and compared with full-wave simulation results and the presented EC model in order to prove the modeling approach.

II. General Antenna Geometry and Its Equivalent Circuit Representation

The antenna presented in this article consists of cascaded building blocks, where the different building blocks, namely the transmission line (TL) sections, the capacitive gap, and the end capacitance, will be characterized and transferred into EC models. An antenna example consisting of four capacitive gaps, which are embedded in a microstrip resonator, is depicted in Fig. 1. The microstrip antenna is built up in the Infineon B11HFC silicon–germanium (SiGe) technology using the uppermost aluminum and the lowermost copper layer as the ground plane for the TL parts and overlapping, floating copper patches for the capacitive gap, all of them embedded in SiO_2. While the end capacitance built by the fringing fields of the microstrip line is the main radiation contribution of ordinary patch antennas [21, p. 835], this antenna mainly radiates by the discontinuity in the TL introduced by the capacitive

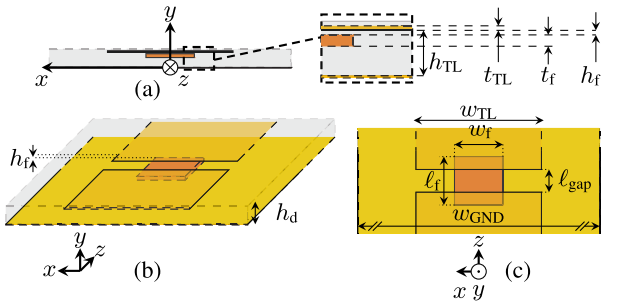

Fig. 2. Schematic drawing of the capacitively coupled gap in (a) cross section and detailed stack information, (b) perspective view, and (c) top view with the dimensions used throughout.

gaps. In general, neither the idea of radiating by microstrip discontinuities nor the simplified modeling and resulting design guidelines of microstrip antennas are new [22], [23]. However, this article aims for a full EC description, allowing antenna design based on circuit simulations. If the antenna is designed as a periodic repetition of unit cells, a dispersion diagram analysis is possible [24], where it can be shown that, generally speaking, an increased number of gap capacitances and a smaller capacitive coupling have the tendency of decreasing the antenna bandwidth [7]. In general, the capacitance of a gap partly compensates the phase shift of a TL section, which means that they can be used to increase the length of the resonators while maintaining a $\lambda/2$-resonance. As a consequence, there exists the following tradeoff in the design process. On the one hand, each capacitance results in a further radiation contribution, which means that the radiation efficiency can be increased by inserting gap capacitances into the resonator. On the other hand, each capacitance also demands a TL section to counteract the phase compensation, and the losses introduced by the TL may overcompensate for the efficiency gain achieved by the capacitive gap. In summary, the optimization process balances the efficiency tradeoff between desirable capacitive gaps and necessary TL sections.

Fig. 1(a) shows the perspective, and Fig. 1(b) shows the top view of the antenna example, respectively, whereas Fig. 1(c) depicts the EC model built up by cascading different building blocks. The building blocks of the model are explicitly labeled in both geometry and EC, but the antenna feeding is not part of the modeling. Since the EC reflects the geometrical outline of the antenna, the cascade of elements in the geometry is visual also in the EC. The antenna can be interpreted as the periodic cascade of unit cells, and a unit cell of length ℓ_{UC} is labeled as well. In this illustration, only the single-ended feeding is shown; however, a symmetric, differential feeding is feasible, as it has been shown to increase the bandwidth and symmetrize the radiation pattern of microstrip antennas [25]. Fig. 2 labels the dimensions of the antenna at a slice of the antenna, including the capacitive gap from different perspectives. The Swiss cheese structure, namely adding holes in the metal layer to fulfill density design rules of the SiGe technology, applied to the floating layer of the capacitive gap is not depicted in Figs. 1 and 2 for reasons of clarity; however, it is included in every simulation. Thus, the modeling is expected to

TABLE I
DIMENSIONS OF THE ANTENNA GIVEN IN FIG. 2

t_{TL}	h_{TL}	w_{TL}	w_{GND}	h_{d}
$0.9\,\mu$m	$9.5\,\mu$m	$83\,\mu$m	$250\,\mu$m	$11.5\,\mu$m
ℓ_{gap}	t_{f}	h_{f}	w_{f}	ℓ_{f}
$15\,\mu$m	$3\,\mu$m	$0.45\,\mu$m	$27.5\,\mu$m...$33\,\mu$m	$34.6\,\mu$m

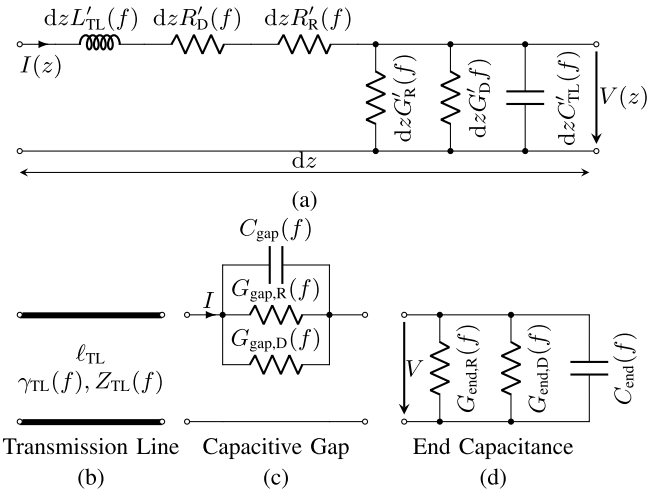

Fig. 3. EC models of the cascaded building blocks utilized, namely (a) TL of infinitesimal length $\mathrm{d}z$, (b) its representation by the length, the complex propagation constant, and characteristic impedance, and (c) capacitive gap and (d) end capacitance.

represent the fabricated chip satisfying the restrictions of the fabrication process. All corresponding dimensions are given in Table I.

The detailed EC models of the building blocks, including the nomenclature of the circuit elements, are depicted in Fig. 3. Here, the resistances or conductances corresponding to a dissipative loss mechanism are highlighted by the index D, whereas the radiation contributors are highlighted by the index R. In contrast to earlier modeling of microstrip gaps [26], the gap utilized here is modeled as a simple series admittance instead of a Π-equivalent due to the dominant series capacitance. Furthermore, it is defined with zero geometrical length instead of its physical extend [27], meaning that the reference plane for incoming and outcoming waves is coincident at the center of the gap. For the gap conductance, the separation of power radiated into free space and into surface waves [28] is not carried out, as the substrate is electrically thin. If a thicker substrate with a significant surface wave loss was used, this should be considered as an additional loss in the modeling of the EC and in the extraction process. The end capacitance could be modeled by an extension length [29]; nevertheless, the separation into an own capacitance and conductance eases building up the EC out of building blocks. By these choices, both capacitances are represented in the EC as a concentrated element; and the phase shift associated with such an element is only defined by its impedance and the environment that it is embedded in, but not by wave-propagation. This eases the definition of the EC, as each TL has the length ℓ_{UC} regardless of the length of the capacitive gap.

Section III will simplify the EC representation by approximations in order to give closed formulas enabling initial

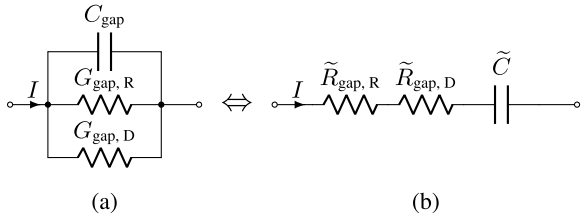

Fig. 4. EC model of the capacitive gap based on (a) physical interpretation and (b) conversion to series elements to ease further analytical calculations.

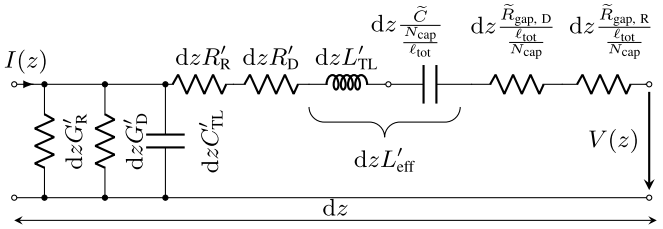

Fig. 5. EC model of the homogenized infinitesimal small TL, including both the elements of the right-handed TL and the series representation of the capacitive gap from Fig. 4.

antenna designs, which can be used as starting values for the circuit simulation-based antenna design process.

III. Analytical Model of Homogenized Antenna

In this section, the analytical estimation of the necessary total antenna length ℓ_{tot} for a half-wavelength current distribution and resulting antenna efficiency is derived. The idea behind this approach is converting the unit cell consisting of both a TL [see Fig. 3(b)] and the capacitive gap [see Fig 3(c)] into a homogenized TL model, neglecting the influence of the fringing fields at the end of the resonator, namely the end capacitance. It should be noted that the homogenization, which is in principle comparable to [24, p. 79], neglects the influence of the actual discrete placement. The effect of this simplification will be discussed in Section V. As this calculation only aims for the half-wavelength resonance, the desired resonance frequency f_0 and the corresponding angular frequency ω_0 are considered here.

First, the finite number of capacitive gaps N_{cap} is distributed along the antenna length ℓ_{tot} in a homogeneous, thus equidistant manner representing quantitatively the original discrete distribution of gaps. Since the capacitive gap is a series element, its shunt-representation will be transformed into a series representation (see Fig. 4) easing further calculations. Second, these series elements will then be transformed into an element per unit length by distributing them along the length $\ell_{\mathrm{tot}}/N_{\mathrm{cap}}$ [24, p. 82]. The transformation from shunt to series elements is equal for G_R and G_D and analogous for C_{gap} according to

$$\widetilde{C} = \frac{(G_R + G_D)^2 + \left(\omega_0 C_{\mathrm{gap}}\right)^2}{\omega_0^2 C_{\mathrm{gap}}} \tag{1}$$

$$\widetilde{R}_{R/D} = \frac{G_{R/D}}{(G_R + G_D)^2 + \left(\omega_0 C_{\mathrm{gap}}\right)^2}. \tag{2}$$

The series elements are denoted by a tilde in order to distinguish them from the shunt elements, and the resulting homogenized EC is depicted in Fig. 5. Here, the series path

of the TL contains both radiation and dissipation losses, as well as the phase shift of the capacitive gap. To consider the phase shift per unit cell caused by the series capacitance, an effective series inductance per unit length consisting of both the homogenized gap capacitance and the inductance per unit length is calculated in accordance with [24, p. 76] to

$$L'_{\text{eff}} = \frac{\mathrm{j}\omega L'_{\text{TL}} + \frac{N_{\text{cap}}}{\mathrm{j}\omega \widetilde{C} \ell_{\text{tot}}}}{\mathrm{j}\omega} = L'_{\text{TL}} - \frac{N_{\text{cap}}}{\omega^2 \widetilde{C} \ell_{\text{tot}}} \tag{3}$$

which can be used with the following abbreviative variables:

$$G'_{\text{TL}} = G'_R + G'_D \tag{4}$$

$$R'_{\text{TL}} = R'_R + R'_D \text{ and} \tag{5}$$

$$\widetilde{R}' = \frac{N_{\text{cap}}}{\ell_{\text{tot}}} \left(\widetilde{R}_{\text{gap},R} + \widetilde{R}_{\text{gap},D} \right) \tag{6}$$

to calculate both the complex propagation constant and the characteristic impedance of the homogenized model

$$\gamma_{\text{UC, hom}} = \sqrt{\left(G'_{\text{TL}} + \mathrm{j}\omega C'_{\text{TL}} \right) \left(R'_{\text{TL}} + \widetilde{R}' + \mathrm{j}\omega L'_{\text{eff}} \right)} \tag{7}$$

$$Z_{\text{UC, hom}} = \sqrt{\frac{R'_{\text{TL}} + \widetilde{R}' + \mathrm{j}\omega L'_{\text{eff}}}{G'_{\text{TL}} + \mathrm{j}\omega C'_{\text{TL}}}}. \tag{8}$$

The length ℓ_{tot} necessary to achieve a $\lambda/2$-resonance (total phase shift of π) can be estimated by

$$\ell_{\text{tot}} = \frac{\pi}{|\operatorname{Im}\{\gamma_{\text{UC, hom}}\}|} \tag{9}$$

and the imaginary part of the propagation constant can be approximated by the phase constant of the lossless unit cell

$$\operatorname{Im}\{\gamma_{\text{UC, hom}}\} \approx \omega_0 \sqrt{C'_{\text{TL}} \left(L'_{\text{TL}} - \frac{N_{\text{cap}}}{\omega_0^2 \widetilde{C} \ell_{\text{tot}}} \right)} \tag{10}$$

where the effective inductance from (3) has been inserted. If (10) is plugged in (9), the result is a quadratic equation with respect to ℓ_{tot}, which can be solved to only positive lengths to

$$\ell_{\text{tot}} = \frac{N_{\text{cap}}}{2\omega_0^2 \widetilde{C} L'_{\text{TL}}} + \frac{1}{\omega_0} \sqrt{\frac{N_{\text{cap}}^2}{4\omega_0^2 \widetilde{C}^2 L'^2_{\text{TL}}} + \frac{\pi^2}{C'_{\text{TL}} L'_{\text{TL}}}}. \tag{11}$$

This length can be used to estimate the total length of a capacitively enhanced microstrip antenna with a number of N_{cap} capacitive gaps if the inductance and capacitance per unit length L'_{TL} and C'_{TL} of the TL, as well as the capacitance of the gap $\widetilde{C}$, are known. As the gap investigated here is mostly capacitive, which means that radiation and dissipation conductances are much smaller compared with the susceptance, one can assume that $\widetilde{C} \approx C_{\text{gap}}$, which means that the length estimation can be carried out even without the extraction of radiation and dissipation losses. The TL parameters can be estimated by any of the available analytical equations [29]–[32].

Finally, assuming a resonant current distribution and knowing the dissipative and radiative EC elements from Fig. 5, the radiation efficiency of the antenna can be estimated as well. In this case, the radiation by the end capacitances and the discrete placement of the gap capacitances are neglected. The voltage and current along with the open-ended TL, given by [33, pp. 60], can be used to calculate the loss contribution. To simplify the calculation, it is assumed that ℓ_{tot} fulfills (9), which means that the half-wavelength resonance results in an integration of the phase angle φ over the antenna length with the integration bounds $0 \leq \varphi \leq \pi$. This means that each series element contributes to radiation (R'_R and $\widetilde{R}'_{\text{gap},R}$) or dissipation ($R'_D$ and $\widetilde{R}'_{\text{gap},D}$) according to

$$P_{\text{Ser}} = R'_{\text{Ser}} \int_0^{\pi} \frac{2|V_0^+|^2}{\operatorname{Im}\{\gamma_{\text{UC}}\}|Z_{\text{UC}}|^2} \sin^2(\varphi) \mathrm{d}\varphi. \tag{12}$$

In the same way, each shunt element contributes to radiation (G'_R) or dissipation (G'_D) according to

$$P_{\text{Shunt}} = G'_{\text{Shunt}} \int_0^{\pi} \frac{2|V_0^+|^2}{\operatorname{Im}\{\gamma_{\text{UC}}\}} \cos^2(\varphi) \mathrm{d}\varphi. \tag{13}$$

Both integrations result in the same expressions except for the term $|Z_{\text{UC}}|^2$, which represents the squared ratio of traveling-wave voltage to current, thus enabling a comparison of power loss of shunt and series elements. The radiation efficiency, dividing the radiated power by all power contributions, can be written as

$$\eta_{\text{Rad}} = \frac{\frac{\widetilde{R}'_{\text{gap},R} N_{\text{cap}}}{\ell_{\text{tot}}|Z_{\text{UC}}|^2} + G'_R}{\frac{\left(\widetilde{R}'_{\text{gap},R} + \widetilde{R}'_{\text{gap},D} \right) N_{\text{cap}}}{\ell_{\text{tot}}|Z_{\text{UC}}|^2} + \frac{R'_R + R'_D}{|Z_{\text{UC}}|^2} + G'_R + G'_D}. \tag{14}$$

As will be shown later, the radiation contributions of the TL are negligible ($R'_R \approx 0$ and $G'_R \approx 0$), and thus

$$\eta_{\text{Rad}} \approx \frac{\frac{\widetilde{R}'_{\text{gap},R} N_{\text{cap}}}{\ell_{\text{tot}}}}{\frac{\left(\widetilde{R}'_{\text{gap},R} + \widetilde{R}'_{\text{gap},D} \right) N_{\text{cap}}}{\ell_{\text{tot}}} + R'_D + |Z_{\text{UC}}|^2 G'_D} \tag{15}$$

can be used. In Section IV, the extraction of the EC parameters will be explained in detail. This enables the analytical calculation of a capacitively enhanced antenna based on the equations presented within this section and allows for a comparison to full-wave simulations to prove both the calculations and the EC model.

IV. Extraction of Frequency-Dependent Equivalent Circuit Parameters

To enable not only the extraction but also the physical interpretation of EC elements, each EC element is extracted with arbitrary frequency dependence, which means that the data sets of different frequencies will be extracted separately. Even though this allows, in general, for element values with fluctuations over frequency, one would expect parameters with physically sound frequency dependencies. If expected frequency dependence will be confirmed, future extraction processes could reduce the number of extraction points by assuming this frequency dependence, as long as nonresonant building blocks are characterized. Otherwise, the EC model needs to be expanded to model, e.g., the inductance of the capacitive gap. The extraction methods applied to the different building blocks, i.e., the TL section, the capacitive gap, and the end capacitance, are presented in the following. All of them utilize a combination of port-based parameters

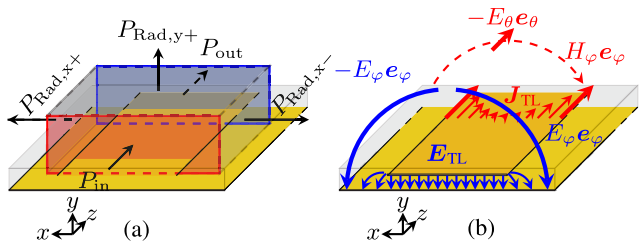

Fig. 6. Schematic drawing of the TL with (a) near-field recording box for the calculation of loss and radiation contributions and (b) radiated electric field in azimuthal direction caused by an applied voltage (blue) and the radiated electric field in elevation direction caused by a current (red).

(e.g., Z-, Y-, and S-parameters) and integrals over near-field data (e.g., power flow) to model the correct impedance behavior while separating the different loss mechanisms. This extraction of different loss parameters is the essential advantage over the design equations for microstrip lines, e.g., from [29].

A. Transmission Line Parameters

As indicated in Fig. 3(a), the EC of the TL is characterized by six elements, which depends, in general, on the geometry and material properties. Although the elements within the EC assume an infinitesimal small piece of TL, the extraction is carried out based on a finite geometrical length ℓ_{TL}. In a full-wave FDTD simulation, a TL of length 1000 μm in the z-direction is excited at one side. The TL guides the excited wave into a perfectly matched layer (PML), assuring that there exist only traveling and no standing waves. Thus, the input impedance at the exciting port is equal to the characteristic impedance Z_{TL} of the TL, as the PML represents an ideal match. Two reference planes with a distance of 350 μm are used to measure the traveling wave voltage and current, resulting in frequency-dependent phase and attenuation information along the 350-μm long part of the TL, which, in combination, can be related to the complex propagation constant γ_{TL}. For the detailed assessment of dissipation and radiation contributions, the near-field data need to be incorporated to extract the EC elements related to the different loss mechanisms. In Fig. 6(a), the near-field recording box calculating the incident and transmitted power guided by the TL at the red and blue surfaces, respectively, is shown. The radiated power in the different directions ($y+, x\pm$) is evaluated at the gray surfaces, and the difference between the incident power and the transmitted/radiated power is equal to the dissipated power in the TL section. After calculating the power balance of this near-field recording box based on the Poynting theorem [33, p. 26], the relation of radiated to dissipated power is known. As the EC differentiates between voltage driven and current driven loss mechanisms, namely conductances and resistances, both the radiation and the dissipation losses need to be separated. The dissipative loss along the TL can occur due to losses within the conductor, which increases roughly proportional to $\sqrt{f}$ [34], and due to the losses within the dielectric, which are expected to be proportional to f, according to a constant $\tan\delta$. To separate both dissipative mechanisms, the volumetric power loss density within the cross section of the TL needs to

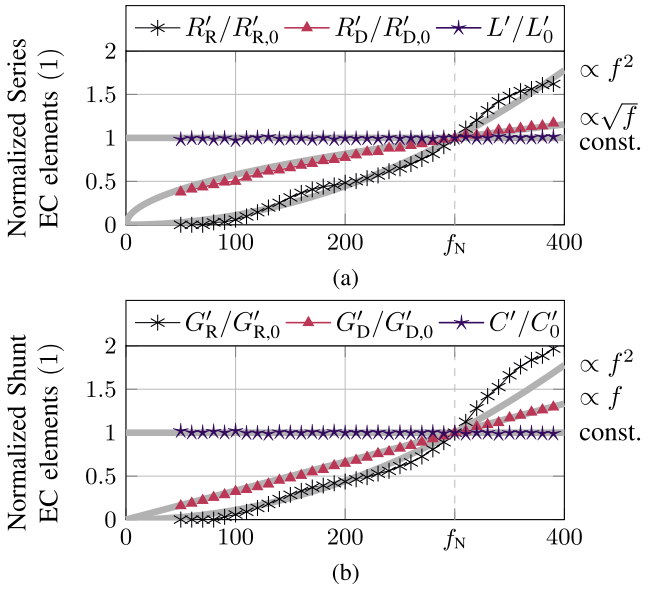

Fig. 7. Normalized EC elements of the TL. (a) Elements of the series path. (b) Elements of the shunt path. All elements are normalized to their respective values at $f_N = 300$ GHz, which are given in Table II.

be integrated over the areas corresponding to dielectric (A_{diel}) or conducting (A_{cond}) media according to

$$P'_{\mathrm{cond}} = \frac{1}{2}\iint_{A_{\mathrm{cond}}} \sigma \|\boldsymbol{E}\|^2 \mathrm{d}A \tag{16}$$

$$P'_{\mathrm{diel}} = \frac{1}{2}\iint_{A_{\mathrm{diel}}} \omega\varepsilon'' \|\boldsymbol{E}\|^2 \mathrm{d}A. \tag{17}$$

In such a way, both losses per unit length can be divided by the squared absolute current or voltage along the line to calculate the corresponding dissipation resistance R'_D and conductance G'_D representing the conductor loss and the dielectric loss, respectively. Furthermore, Fig. 6(b) shows the electric field components that are assumed to be the dominant ones given either a shunt voltage (E_φ, drawn in blue) or a series current (E_θ, drawn in red) as a radiation source. The total radiated power is assigned to voltage- and current-driven radiation sources based on the ratio of power corresponding to the E_φ and E_θ radiations, respectively. Finally, these weighted parts of the radiated power are related to a loss integral of the squared absolute current or voltage to calculate the radiation resistance R'_R and conductance G'_R. Since the propagation constant of the TL is already known, the evaluation of the loss integral is straightforward.

To find a suitable EC model considering the different abovementioned parameters, a genetic algorithm representing the EC elements by gray-coded parameters [35, p. 100] has been used to determine the EC with the best value of the fitness function, where the fitness function is a weighted sum of the relative deviations of propagation constant, characteristic impedance, and loss contributions between the circuit and full-wave simulation. As stated earlier, this optimization is carried out for each frequency independently. Fig. 7 represents the extracted EC elements normalized to their respective value at $f_N = 300$ GHz. In this way, different units and orders of magnitude can be compared concerning their frequency

TABLE II
EC ELEMENTS OF THE TL AT $f_N = 300$ GHz

	FDTD-Extr.	FEM-Sim.	Analytical (cf. [32])
$R'_{\mathrm{D},0}$ (kΩ/m)	3.072	2.827	–
$R'_{\mathrm{R},0}$ (Ω/m)	2.482	–	–
$G'_{\mathrm{D},0}$ (S/m)	0.4447	0.4682	0.5099
$G'_{\mathrm{R},0}$ (mS/m)	16.65	–	–
L'_0 (nH/m)	113.1	102.0	117.9
C'_0 (nF/m)	0.3686	0.3992	0.3864

dependence. The normalizing element values at 300 GHz are given in Table II. The reactive and dissipative elements can also be extracted from a quasi-static 2-D FEM simulation and are given for comparison. In addition, the values calculated analytically by Owens [32] are listed there. Here, extracted elements are in good agreement with the FEM simulation and the analytical calculations. Looking at Fig. 7, different frequency dependencies can be observed. To guide the interpretation, usual dependencies on the frequency are plotted as gray thick lines in the background. Concerning the most dominant elements of the TL, namely its capacitance and inductance per unit length, both behave extraordinarily constant with respect to frequency. The radiative elements show minor undulations but follow, in general, the $\propto f^2$ curve in a good agreement. From the analytical derivation in [22], one would expect for a lossless TEM-line no radiation contribution at all. However, the incorporation of losses yields problems, as any source in an infinite distance would need to impress infinite currents yielding radiation contributions. In [28], it is stated that, even though a uniform line radiates power, nevertheless, the loss due to radiation would be much smaller compared with the dissipative loss. This consistently fits the extracted radiation contributions that are orders of magnitude smaller compared with the dissipative losses. The dominant losses corresponding to conductor loss and dielectric loss follow precisely the expected behavior; namely, the losses within the dielectrics are $\propto f$, and the conductor losses follow the $\sqrt{f}$-proportionality [34]. For future extractions, it is obvious that similar structures can be analyzed only based on the reactive and dissipative elements, which can be calculated by well-documented formulas per se [29], and the radiative elements of the TL can be neglected.

B. Capacitively Coupled Gap

The procedure of extracting the EC elements for the capacitively coupled gap is comparable to the previous extraction, but, here, the EC element is only a series element and, thus, only dependent on the current. In general, the radiation conductance has been derived analytically for generic discontinuities in [36] however, more complicated structures, as presented here, might justify the extraction out of full-wave simulations. Within this publication, two different overlapping areas are extracted as examples, namely $w_f = 27.5$ and 33 μm. In the FDTD simulation, the capacitive gap is located at the center of the already known TL. Two reference planes with a distance of 350 μm centered around the capacitive gap are used for recording two-port parameters, namely the current and voltage assuming a quasi-TEM behavior, and near-field parameters, namely the power flow through the respective side

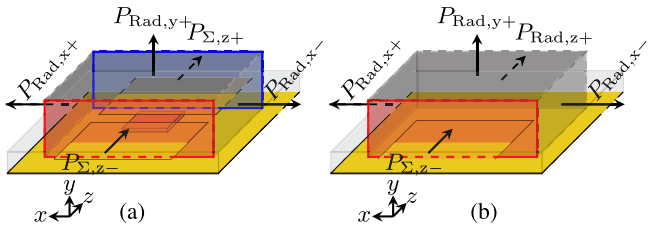

Fig. 8. Schematic drawing of (a) capacitive gap in a perspective view and (b) end capacitance with recording box for the calculation of loss and radiation contributions.

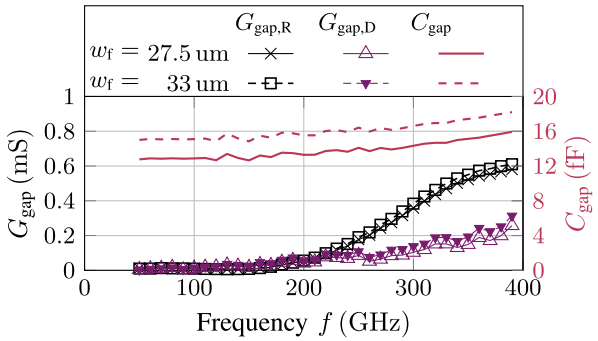

Fig. 9. EC elements for the capacitive gap extracted from the setup depicted in Fig. 8(a) for both widths $w_f \in \{27.5\ \mu\mathrm{m}, 33\ \mu\mathrm{m}\}$.

of the near-field recording box [see Fig. 8(a)]. With the TL parameters extracted earlier, the dominant reactive part C_{gap} can be extracted by deembedding the two-port parameters by a distance of 175 μm per side.

To calculate the radiative and dissipative conductances, $G_{\mathrm{gap},R}$ and $G_{\mathrm{gap},D}$, the radiated and dissipated powers contributions by both the TL and capacitive gap inside the recording box are extracted from the simulation. At the red and blue faces of the near-field recording box (see Fig. 8), the power flow along the TL needs to be separated from the radiated power of the discontinuity by accessing the voltage and current at the reference planes. The difference of the power guided by the TL (P_{in}, P_{out}) and the power flow calculated by the near-fields at the reference planes ($P_{\Sigma,\pm z}$) is associated with the outwards pointing radiation in the $\pm z$-direction ($P_{\mathrm{Rad},\pm z}$) according to

$$P_{\Sigma,\mathrm{z+}} = -P_{\mathrm{Rad,z+}} + P_{\mathrm{in}} \tag{18}$$

$$P_{\Sigma,\mathrm{z-}} = +P_{\mathrm{Rad,z-}} + P_{\mathrm{out}}. \tag{19}$$

All other radiation contributions can be directly extracted from the remaining faces of the near-field recording box. From a circuit simulation, the dissipation and radiation contributions of the TLs can be calculated and used to calculate the radiation and dissipation contributions of the capacitive gap. By utilizing the circuit simulation, the EC elements, $G_{\mathrm{gap},R}$ and $G_{\mathrm{gap},D}$, can be determined from the radiated and dissipated powers, respectively. The extracted EC elements in dependence on the frequency are depicted in Fig. 9. From the extracted elements, one can see that the capacitance is almost constant, whereas both dissipation and radiation losses increase with frequency. The capacitive gap becomes a good radiator above 300 GHz, where the ratio of radiation conductance to dissipation conductance peaks. This ratio could be interpreted as the intrinsic

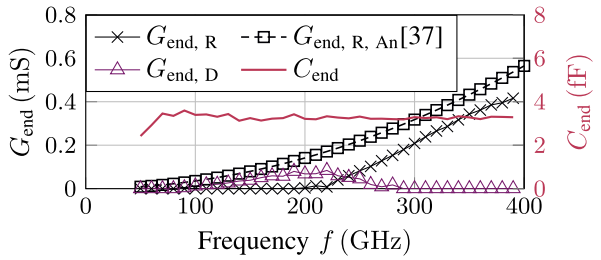

Fig. 10. EC elements for the end capacitance extracted from the setup depicted in Fig. 8(b) and the analytical solution of the radiation conductance according to [37].

radiation efficiency of the capacitive gap

$$\eta_{\text{intr., gap}} = \frac{G_{R,\text{gap}}}{G_{R,\text{gap}} + G_{D,\text{gap}}} \tag{20}$$

which exceeds 0.5 above 220 GHz and is practically an upper bound for the radiation efficiency of the overall antenna if the gap is the main radiation contributor. Finally, the main difference between $w_f = 27.5$ and 33 μm, is the change in the resulting capacitance, whereas the loss and radiation contributions of both are comparable.

C. End Capacitance

The extraction of the EC elements of the end capacitance is carried out similar to the previous method for the capacitive gap. As the main difference, the element investigated here is a one-port element. As it occurred in the previous extraction of the capacitive gap, the capacitance is extracted straightforward from port parameters, whereas the extraction of losses has been carried out using the near-field recording box [see Fig. 8(b)].

Fig. 10 shows the extracted values for both the end capacitance and the dissipation and radiation conductances. The behavior of the radiation conductance appears to be imprecisely extracted, as it starts increasing above 220 GHz rapidly. In addition, the dissipation conductance even decreases around this frequency, which cannot be explained. However, at the operation frequency, it is assumed that the main loss contribution is radiation since dissipation could only occur due to an altered current distribution at the discontinuity [22] and due to dielectric losses, which are negligible in this case. This assumption is supported by the radiation conductance calculated analytically according to [37], which is also depicted in Fig. 10. Here, it can be seen that the extracted radiation conductance is underestimated by the extraction process, implying that the separation of loss and radiation did not work out for frequencies below 200 GHz. The effects of this will be discussed in more detail in Section V.

V. Evaluation of the Presented EC Model Based on Antenna Parameters

To evaluate the accuracy of the EC model, an antenna consisting of $N_{\text{cap}} = 4$ capacitive gaps with $w_f = 27.5$ μm has been designed based on (11). The resulting necessary antenna length was $\ell_{\text{tot}} = 595$ μm for a $\lambda/2$ resonance at $f_0 = 340$ GHz. The analytically estimated radiation efficiency amounts to $\eta_{\text{Rad, An}} = 0.51$ according to (15). With the extracted EC parameters, an EC model can be built up and evaluated. All TL sections are of length $\ell_{\text{TL}} = \ell_{\text{tot}}/5 \approx 119$ μm, and the general EC is already depicted in Fig. 1.

The calculation of port parameters, e.g., the input impedance Z_{in}, can be carried out by cascading ABCD matrices of the different building blocks in the order given by the EC. The calculation of currents and voltages within the EC can be carried out by a circuit simulator. Here, each series element, e.g., the capacitive gap, will alter the voltage, whereas each shunt element, e.g., the end capacitance, will alter the current along with the topology. The TL will alter both based on the well-known TL equations [33, p. 48]. These equations can also be used to obtain the currents and voltages and losses along with the TL. With all currents and voltages calculated, both the input power and the power dissipated or radiated by each element can be accessed. All losses can be sorted by radiation and dissipation yielding the radiation efficiency. In addition to the radiation efficiency and the input impedance, even a rough approximation of the radiation pattern can be calculated by the superposition of far-fields of elementary radiators. Although this method is not a typical application of circuit simulations, the results of this superposition will be referred to as EC since they are based on the power and phase calculation of the circuit simulation. As it will be shown in the next paragraph, the dominant radiation contributors are the capacitive gaps and the end capacitance. The radiation patterns of slot antennas based on a constant field strength within an aperture [38, p. 169] are associated with the geometrical position of the radiation contributors and weighted with the current or voltage phase and the corresponding radiated power. After a straightforward antenna array superposition assuming decoupled radiation contributions [38, pp. 107], the resulting directivity of the antenna can be calculated. Since the cross-polarization cannot be determined by this method, only the copolarization will be presented in the radiation patterns in the following. Because the radiation efficiency is known and the mismatch to a given reference impedance can be calculated, both the antenna gain and the realized gain can be calculated additionally to the directivity. Here, the substrate effect underneath and above the slot [21, pp. 712 and 837] and the finite ground plane is neglected, which will result in inaccurate directivity predictions far off the broadside direction. More accurate predictions can be made by including the substrate effects or directly using simulated far-fields of the building blocks.

First, the EC model will be used to generate further physical insight to understand the radiation mechanism of the antenna. Fig. 11(a) depicts the radiation and dissipation contributions of the different building blocks in a stacked graph. In general, all radiation contributions are in bold colors, whereas all dissipation contributions are desaturated. The vertical position of each contribution corresponds to the geometrical position on the real antenna geometry, which is visualized by the projection of the different contributions onto the antenna's radiation and dissipation contributions on the right-hand side. In detail, each blue contribution is linked to the end capacitance, each black/gray contribution to the TL sections, and each red contribution to the capacitive gaps. The black–white dotted

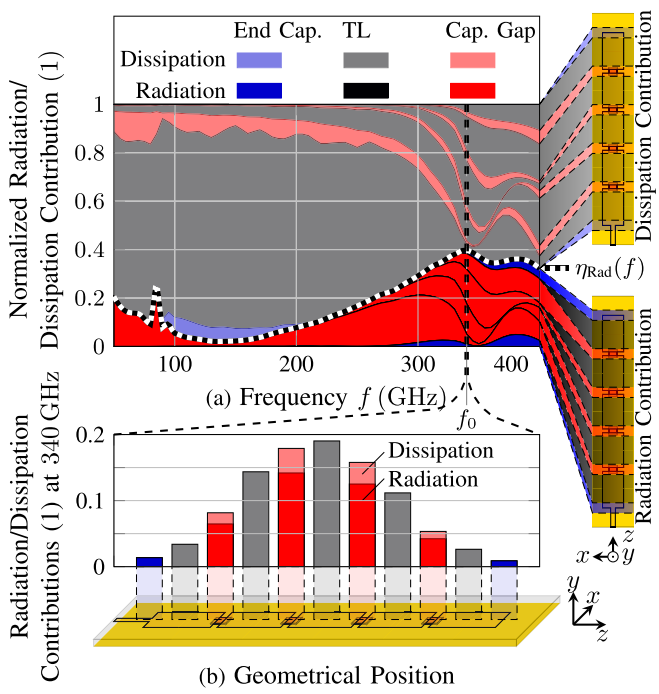

Fig. 11. Estimation of the radiation and loss contributions predicted by the EC (a) as a function of frequency and (b) at 340 GHz related to the geometrical position and the corresponding antenna parts.

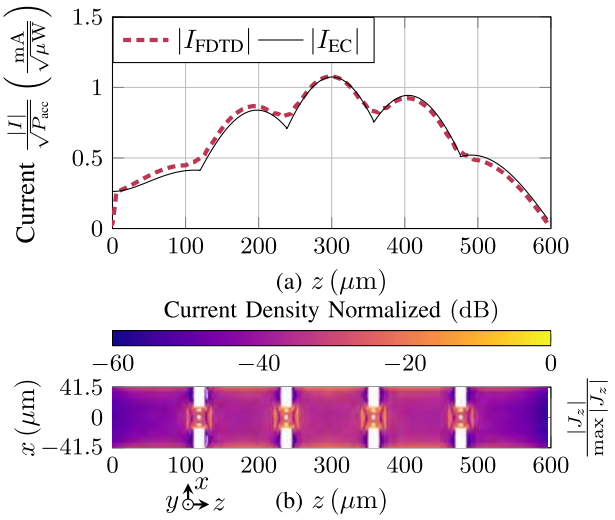

Fig. 12. Resonant half-wavelength current distribution calculated by (a) FDTD simulation and the EC model and (b) simulated current density z-component at 340 GHz projected from both metal layers onto one plane.

line represents the border between radiation and dissipation contributions and is equal to the radiation efficiency. On the one hand, the radiation contributions are dominated by the capacitive gaps highlighted in red, and minor contributions can be assigned to the end capacitances in blue, whereas the radiation contributions of the TLs are practically negligible, and these are marked by the black lines. On the other hand, the dissipation contributions are dominated by both the TLs and the capacitive gaps. At the desired operation frequency of 340 GHz, the radiation efficiency reaches its maximum value of $\eta_{\mathrm{Rad,EC}} = 0.397$. Fig. 11(b) shows the radiation and dissipation contributions of the different building blocks at 340 GHz utilizing the same color scheme, such that the distribution of loss and radiation mechanisms along the geometry of the antenna can be easily seen. As expected for a $\lambda/2$-current distribution, the largest losses occur in the center of the antenna, where the current is maximized. The loss distribution along the antenna is almost symmetrical, but a slight tendency toward the antenna feed on the left-hand side is recognizable. Finally, this figure proves that the discontinuities introduced into the antenna, namely the capacitive gaps, yield additional radiation contributions and, thus, increase the overall radiation efficiency, which has already been claimed in [7].

To prove the applicability of the EC, the results of the circuit simulation will be compared with a full-wave solution obtained by the FDTD-solver EMPIRE XPU. Fig. 12(a) shows the current distribution calculated by the circuit simulation and the full-wave simulation at 340 GHz. To achieve comparability, the current distributions are normalized to the square-root of the accepted power and plotted as a function of z. The current distribution for the FDTD simulation is calculated by integrating the normal component of the current density with respect to the x–y-cross section of the antenna. First, the current distribution predicted by the EC shows an excellent fit with the solution of the full-wave simulation. Small differences occur at the capacitive gaps, where the full-wave results show a smoother local minimum, since the capacitive gap is assumed of zero geometrical length in the EC model. Furthermore, the current drops rapidly at $z \approx 0$ within the FDTD simulation, which can be explained by the finite extent of the lumped port in the z-direction. Fig. 12(b) shows the current density's z-component normalized to the maximum value. To ease the interpretation of the current density at both top layers, the current density is projected into one plane. In total, the half-wavelength current distribution, slightly deformed due to the discontinuities of the capacitive gaps, can be recognized. The overestimation of the radiation efficiency by the analytical solution (15), which resulted in $\eta_{\mathrm{Rad,\,An}} = 0.509$, compared with the efficiency calculated by the EC, $\eta_{\mathrm{Rad,\,EC}} = 0.397$, can be explained by the current distribution. For the analytical estimation, the current distribution has been approximated as ideally sinusoidal; however, the EC and FDTD simulations both show that the current has local maxima along with the TL and local minima at the capacitive gaps. This results in a reduced radiation contribution of the capacitive gaps and an increased dissipation contribution of the TLs, which is not considered in the derivation of (15). The radiation pattern calculated by the superposition of the radiating slots representing the capacitive gaps and end capacitances at 340 GHz is depicted in Fig. 13(a). To ease the description of radiated fields, the coordinate system has been changed, as shown in the inset. Since the effect of the substrate is not included in the radiation pattern of the slots, the estimation of the directivity off broadside direction, i.e., for large angles $|\theta|$, deviates strongly from the full-wave simulation result. However, in the broadside direction, the estimation based on the EC-results and the full-wave simulation agrees very well. While the radiation

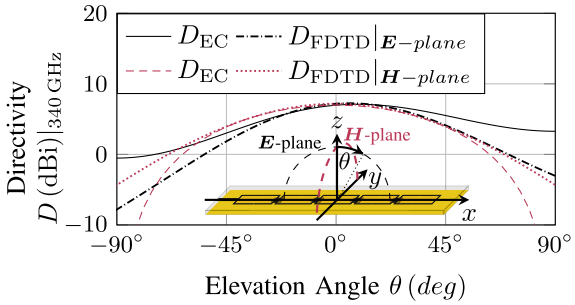

Fig. 13. Radiation pattern calculated from the EC-data and with the FDTD-method. Inset: utilized coordinate system.

pattern is symmetric in the $\boldsymbol{H}$-plane due to the symmetry of the antenna, the $\boldsymbol{E}$-plane shows a slight asymmetry, which means that the radiation pattern calculated by both the EC model and the FDTD-solver are slightly tilted toward the positive θ direction.

To check the accuracy of the EC estimation compared with the full-wave simulation, Fig. 14(a) shows the essential parameters of the far-field, namely the radiation efficiency and the directivity in broadside direction, and Fig. 14(b) depicts the input impedance of the antenna. Within a broad bandwidth around the desired operation frequency, the radiation efficiency, the broadside directivity, and the input impedance in real and imaginary parts are predicted by the EC model with very high accuracy. The antenna efficiency shows significant deviations below 200 GHz, which become larger below 100 GHz. This can be explained by remembering the possibly inaccurate extraction of the end capacitance (see Fig. 10) and can also be seen in the increased dissipation loss predicted for the end capacitance in Fig. 11 (light blue shaded area). It is assumed that the extracted EC-parameters, especially the loss contributing elements, are extracted with a lower precision for the larger wavelengths due to the limited size of the near-field recording boxes. However, the size of the near-field boxes should not be chosen too large, as this size generally increases the TL losses, which complicates the extraction for low-loss building blocks. Nevertheless, close to the desired half-wavelength resonance, the efficiency estimation by the EC is precise. When comparing the directivity obtained from the EC and the full-wave simulation, the prediction is very accurate, except for very low frequencies. Even the broadside null resulting from a full-wavelength current distribution at $\approx$ 390 GHz is predicted precisely. Finally, the input impedance is estimated correctly by the EC in real and imaginary parts for all frequencies.

To summarize this section, all relevant antenna parameters can be predicted precisely by the EC model. The limitations of the model become visible at low frequencies. First, the extraction method relying on fixed-size near-field recording boxes suffers from low frequencies in terms of large wavelengths due to increasing reactive near fields. Second, the coupling between the radiating elements increases with decreasing frequency, as their fixed distance becomes electrically smaller. The EC model assumes that the only coupling between the discontinuities occurs due to the guided-wave

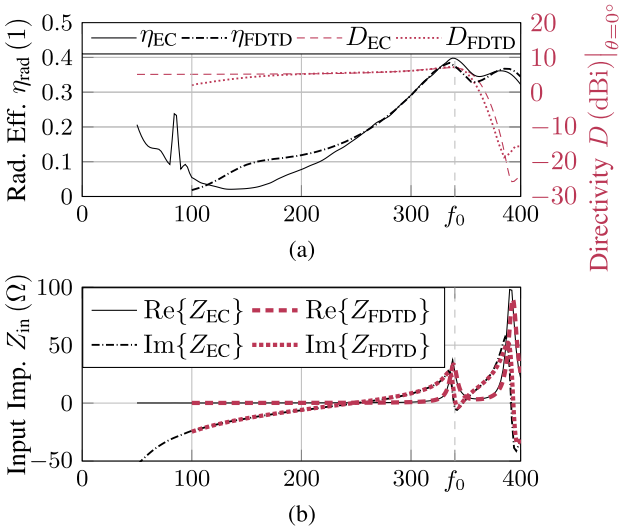

Fig. 14. (a) Radiation efficiency and the broadside directivity and (b) input impedance comparing the EC and FDTD solutions.

within the connecting TL. Any coupling through free-space, which could increase especially for lower frequencies and, thus, geometrically larger reactive near-fields, is not modeled by the EC. Finally, the equation predicting the approximate necessary antenna length (11) resulted in an antenna design operating at 338 GHz, where the maximum of the real input impedance occurred. This is very close to the desired operating frequency of 340 GHz.

VI. On-Chip Antenna Measurements

This section presents a fabricated on-chip antenna utilizing the approach of capacitively enhanced microstrip antennas [7]. The utilized SiGe technology B11HFC features a copper ground layer for the microstrip antenna, where the microstrip itself was fabricated on the aluminum layer and the overlapping capacitances have been created by using the copper layer underneath. Two design mistakes in the full-wave simulation, which concerned the permittivity of a dielectric layer and the electrical length of quarter-wavelength transformers, result in a shifted operation frequency, as will be shown later. Fig. 15 shows an EC model for the antenna assembly and the corresponding realized and simulated antenna in the top view. The general design consists of two antenna pairs, two parallel inner antennas intended to operate at 340 GHz, and two outer antennas with a designed operating frequency of 320 GHz. The different resonance frequencies have been targeted by using different capacitive gaps and slightly different antenna lengths given in Fig. 15(a). The feeding network of all four antennas consists of quarter-wavelength impedance transformers, where the quarter-wavelength relates to the operation frequency of the fed antenna, to transform the local maximum of $Z_{1/2}$ into a local minimum $\tilde{Z}_{1/2}$. The input impedance Z_F resulting from the shunt connection of both antenna pairs is then dominated by the respective smaller impedance, which means that frequency selectivity is an inherent part of the feeding network. This yields the operation of the outer antenna pair around 320 GHz and the operation of the inner antenna pair around 340 GHz. The probing pads are not included in

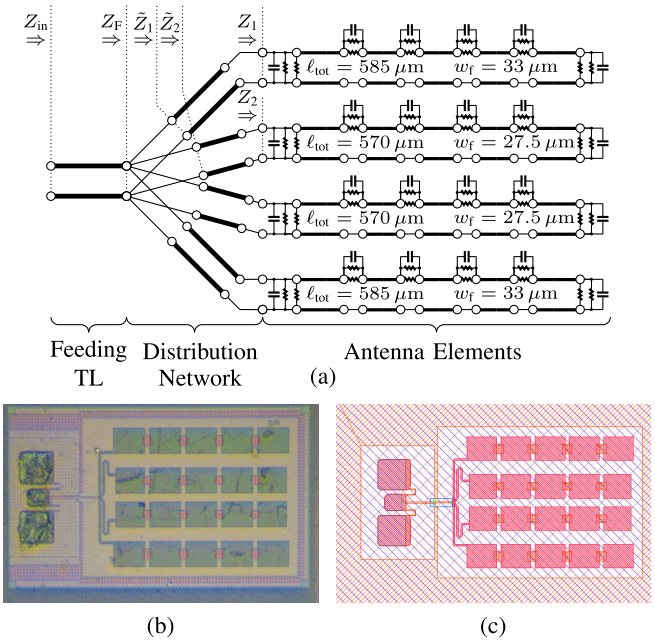

Fig. 15. Antenna assembly consisting of each two different antennas. (a) Full EC model, including the feeding line. (b) Photograph from the on-chip antenna. (c) Antenna modeled in the full-wave simulation software.

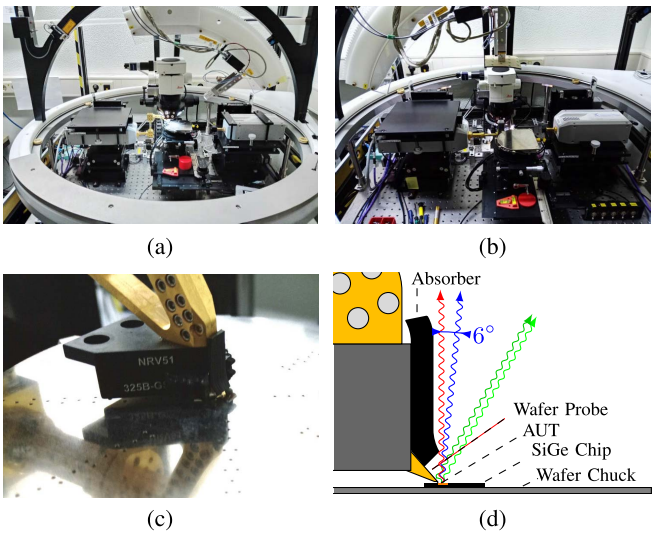

Fig. 16. Photograph of the antenna measurement setup from [39] with the microscope over (a) wafer chuck and (b) within the reference measurement of the horn antenna. (c) Closeup of the on-wafer probe with the mm-wave absorbers. (d) Cross section sketch to indicate the effect of the absorber and the metallic probe.

the EC model, but their influence is approximately included by adding a TL section representing the electrical length between contacting probe tip and feeding line.

Due to a miscalculation during the design process, the desired quarter-wavelength transformers are electrically too long, resulting in missing the desired input impedance level. The intention of this feeding network, to distribute the power frequency dependent, is thus only sub-optimally fulfilled, which decreases the bandwidth covered by the antenna assembly. Furthermore, a thin passivation SiN-layer between the uppermost metal layers has been underestimated in its effect. For the patch antennas utilized usually, this layer is negligible. Since the presented antenna includes coupling capacitances utilizing this layer, it is extraordinarily sensitive to the permittivity of this layer. As a consequence, the operation frequency of each antenna pair will be decreased to 295 and 305 GHz. To account for this effect, the EC-extraction process has been carried out again, including the SiN-layer in the full-wave simulations and, thus, in the EC model. The results presented from now on are based on the corrected EC model. For the on-chip antenna measurement, the spherical antenna measurement system presented in [39] was set up to measure the copolarization of the antenna. The measurement setup with the microscope over the wafer chuck and the reference horn antenna is depicted in Fig. 16(a) and (b), respectively. To reduce the effect of the metallic on-wafer probe on the measured radiation pattern, its frontside facing the antenna was covered with an mm-wave absorber [see Fig. 16(c)]. The effect of the absorber and the metallic probe is sketched in Fig. 16(d). Due to the proximity of absorber and antenna, the radiated far-field in the broadside direction ($\theta = 0°$, marked with the red line) is attenuated, thus no reliable measure for the antenna's gain. Since the antenna has a relatively large beamwidth, the antenna gain will be measured at a slightly tilted angle ($\theta = 6°$, marked with the blue line), where the effect of the absorber is assumed to be negligible. It should be noted that the uncovered parts of the probe might still change the radiation pattern due to interference, as indicated with the green lines (transmitted by the antenna and reflected from the probe) in Fig. 16(d). Since the effect of the wafer probe is an artifact of the measurement and, thus, not included in the far-field calculated by the EC model, the validation of the model will be carried out in two steps. First, the antenna gain calculated by the full-wave FDTD simulation will be compared with the antenna gain predicted by the EC model, both without the effect of the wafer probe. Second, the antenna gain measured with the setup will be compared with the gain calculated by the full-wave simulation, both including the uncovered-part of the wafer probe. In Fig. 17(a), the EC predicts both a steeper increasing gain toward the operation frequency but also a lower gain compared with the full-wave simulation. The utilized EC model neglects both the coupling between the antennas and undesired radiation contributions from the feeding network, e.g., from microstrip bends. These neglected effects are identified to explain the difference to the full-wave simulations, as the single antenna element has been described by the EC with very good accuracy (see Section V). Here, only the gain, not the realized gain, is shown to exclude the impedance mismatch, as the EC uses only a simple TL to model the probing pads. Considering this simple modeling, the input impedance in Fig. 17(c) shows a good agreement between the EC model and the measured input impedance. Around the operation frequency of the antennas, a more capacitive behavior resulting in an increased reflection coefficient is calculated by the circuit simulation compared with the on-chip measurement. As explained earlier, the design error concerning the SiN-layer and the erroneous length of the quarter-wavelength transformers results in both detuned

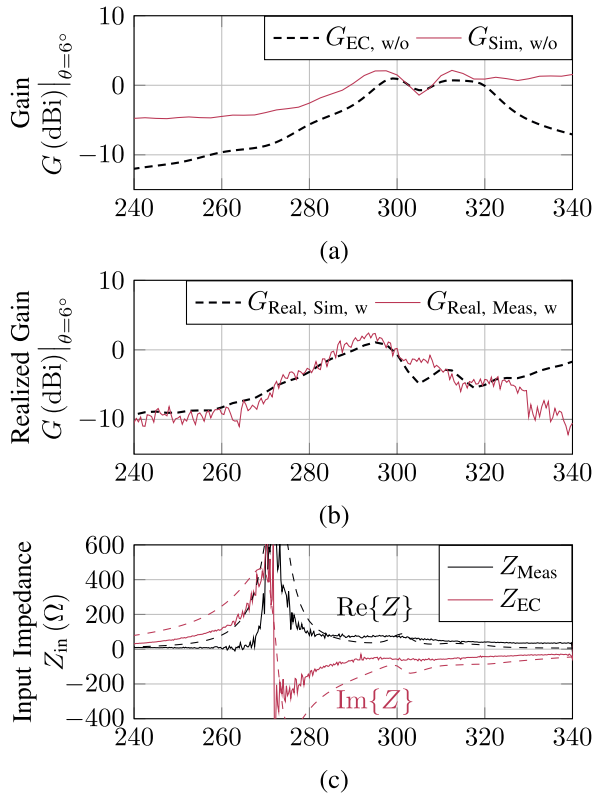

Fig. 17. Antenna measurement and simulation comparing (a) gain without the effect of the probe tip (w/o) for EC and full-wave solution, (b) realized gain including the effect of the probe tip (w) comparing the full-wave solution and the measurement, and (c) input impedance at the probe pads for EC and measurement.

antennas and not well-matched input impedance. Furthermore, Fig. 17(b) compares the realized gain of simulation and measurement, including the effect of the probe tip. Here, a very good agreement between simulation and measurement can be shown. The realized gain has been calculated based on the gain of a reference horn antenna [see Fig. 16(b)], including the compensation for the losses of the wafer probe and the additionally inserted waveguide sections [40]. Both the measured and simulated realized gain peak at 295 GHz, where the measured gain is even larger compared with the simulated gain. In contrast to that, the simulated antenna with the probe tip predicts a drastically decreased gain at 305 GHz, which can neither be seen at the measurement result nor at the gain of the antenna without probe tip [see Fig. 17(a)]. Here, it appears that the modeling of the metallic on-wafer probe in the full-wave simulation is not ideal, resulting in different interference effects in the simulation and the measurement. To prove this hypothesis, $\boldsymbol{E}$- and $\boldsymbol{H}$-planes have been measured and are shown in Fig. 18 for 295 and 305 GHz. While the agreement between simulation and measurement is acceptable for 295 GHz, strong deviations between both results can be seen at 305 GHz. It should be emphasized that the antenna is influenced by the metallic probe tip and that the differences observed are due to the modeling of the probe tip in the full-wave simulation, which seems not sufficiently detailed.

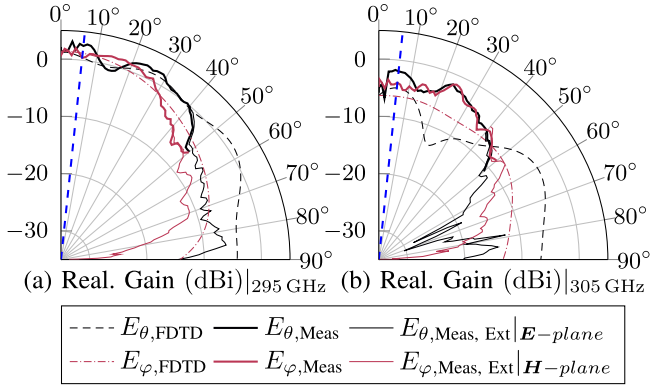

Fig. 18. Comparison of measured and simulated radiation pattern, including the influence of the probe tip at (a) 295 and (b) 305 GHz. Only each half cut-plane is shown, as the negative $\boldsymbol{E}$-plane is obscured by the probe, and the $\boldsymbol{H}$-plane should be symmetric. The blue line highlights the tilted angle explained in Fig. 16 (d) and used in Fig. 17(a) and (b).

In conclusion, the good agreement between the measured and simulated gains over the operating bandwidth implies two key outcomes. First, the consideration of the SiN layer within the simulation is crucial for this antenna type and needs to be included in the extracted EC models. Second, from the good agreement of the realized gain for measurement and simulation, one can conclude that directivity, impedance mismatch, and radiation efficiency calculated by the FDTD simulation are correct. Furthermore, given that coupling effects have been neglected, the gain calculated by the EC model of the antenna assembly matches the simulation result well. Finally, even the input impedance estimated by the EC is in good agreement with the on-chip measurement. This implies that the modeling of materials, conductor, and dielectric losses within the FDTD simulation and extracted EC are still valid at mm-wave frequencies, even for complicated antenna structures.

VII. Conclusion

This article has presented an EC to model microstrip-based antennas supplemented with series capacitances. The modeling of the utilized antenna parts is based on the extraction of EC parameters from full-wave simulations while separating radiation and dissipation mechanisms. Each of the EC models describes a specific antenna part, and being cascaded, they model the antenna assembly. The resulting EC model can be used to calculate the antenna efficiency, input impedance, and broadside gain in excellent agreement with the full-wave simulation results. Furthermore, this EC model allows for initial analytical considerations based on a homogenized antenna model easing the design process by a presented design rule. Consequently, a computationally efficient calculation of antenna parameters using only a circuit simulation can be carried out in the order of seconds, which is an essential improvement compared with structural efficient, but still long-lasting FDTD simulations in the order of hours. Based on this fast antenna characterization, an EC-based antenna optimization for maximized radiation efficiency with the constraints of on-chip antennas is conceivably possible.

To verify the radiation efficiency calculated by the FDTD simulation and prove that the modeling of conductor and dielectric losses has been carried out thoroughly, an mm-wave on-chip antenna has been fabricated. Here, a very good agreement between the measured and simulated realized gains has been achieved after correcting two design mistakes. Furthermore, the EC model of the array assembly is in good agreement with the full-wave simulation results, despite that antenna-to-antenna coupling is not included in the EC model. Thus, it is claimed that both the FDTD simulation and the EC model are valid representations of real on-chip antennas. Based on the extraction method yielding the EC model, further efficiency optimization, increased physical insight, and more advanced antenna designs can be developed systematically.

ACKNOWLEDGMENT

The authors are grateful to Infineon Technologies AG for manufacturing and providing the test chip with the on-chip antenna and Klaus Aufinger, Infineon Technologies, for his extensive and valuable consultation.

REFERENCES

[1] T. Jaeschke, C. Bredendiek, and N. Pohl, "A 240 GHz ultra-wideband FMCW radar system with on-chip antennas for high resolution radar imaging," in *IEEE MTT-S Int. Microw. Symp. Dig.*, Jun. 2013, pp. 1–4.

[2] G. P. Kniffin and L. M. Zurk, "Model-based material parameter estimation for terahertz reflection spectroscopy," *IEEE Trans. THz Sci. Technol.*, vol. 2, no. 2, pp. 231–241, Mar. 2012.

[3] K. K. Tokgoz *et al.*, "A 120 Gb/s 16 QAM CMOS millimeter-wave wireless transceiver," in *IEEE Int. Solid-State Circuits Conf. (ISSCC) Dig. Tech. Papers*, Feb. 2018, pp. 168–170.

[4] T. Hirano, K. Okada, J. Hirokawa, and M. Ando, "60 GHz on-chip patch antenna integrated in a 0.18-μm CMOS technology," in *Proc. Int. Symp. Antennas Propag. (ISAP)*, Nagoya, Japan, Oct. 2012, pp. 62–65.

[5] R. Han *et al.*, "A 280-GHz Schottky diode detector in 130-nm digital CMOS," *IEEE J. Solid-State Circuits*, vol. 46, no. 11, pp. 2602–2612, Nov. 2011.

[6] Z. Chen, C.-C. Wang, H.-C. Yao, and P. Heydari, "A BiCMOS W-band 2×2 focal-plane array with on-chip antenna," *IEEE J. Solid-State Circuits*, vol. 47, no. 10, pp. 2355–2371, Oct. 2012.

[7] B. Sievert, D. Erni, and A. Rennings, "Resonant antenna periodically loaded with series capacitances for enhanced radiation efficiency," in *Proc. 12th German Microw. Conf. (GeMiC)*, Stuttgart, Germany, Mar. 2019, pp. 20–23.

[8] T. Zwick, D. Liu, and B. P. Gaucher, "Broadband planar superstrate antenna for integrated millimeterwave transceivers," *IEEE Trans. Antennas Propag.*, vol. 54, no. 10, pp. 2790–2796, Oct. 2006.

[9] S. Beer, H. Gulan, C. Rusch, and T. Zwick, "Coplanar 122-GHz antenna array with air cavity reflector for integration in plastic packages," *IEEE Antennas Wireless Propag. Lett.*, vol. 11, pp. 160–163, Mar. 2012.

[10] B. Klein, R. Hahnel, and D. Plettemeier, "Dual-polarized integrated mmWave antenna for high-speed wireless communication," in *Proc. IEEE-APS Topical Conf. Antennas Propag. Wireless Commun. (APWC)*, Cartagena des Indias, Columbia, Sep. 2018, pp. 826–829.

[11] P. V. Testa, B. Klein, R. Hannel, C. Carta, D. Plettemeier, and F. Ellinger, "Distributed power combiner and on-chip antennas for sub-THz multi-band UWB receivers," in *Proc. IEEE Int. RF Microw. Conf. (RFM)*, Penang, Malaysia, Dec. 2018, pp. 139–142.

[12] D. L. Cuenca, J. Hesselbarth, and G. Alavi, "Chip-mounted dielectric resonator antenna with alignment and testing features," in *Proc. 46th Eur. Microw. Conf. (EuMC)*, London, U.K., Oct. 2016, pp. 723–726.

[13] B. Sievert, J.-T. Svejda, D. Erni, and A. Rennings, "Mutually coupled dielectric resonators for on-chip antenna efficiency enhancement," in *Proc. 2nd Int. Workshop Mobile THz Syst. (IWMTS)*, Bad Neuenahr, Germany, Jul. 2019, pp. 1–4.

[14] C.-H. Li and T.-Y. Chiu, "340-GHz low-cost and high-gain on-chip higher order mode dielectric resonator antenna for THz applications," *IEEE Trans. THz Sci. Technol.*, vol. 7, no. 3, pp. 284–294, May 2017.

[15] M. Uzunkol, O. D. Gurbuz, F. Golcuk, and G. M. Rebeiz, "A 0.32 THz SiGe 4×4 imaging array using high-efficiency on-chip antennas," *IEEE J. Solid-State Circuits*, vol. 48, no. 9, pp. 2056–2066, Sep. 2013.

[16] D. L. Cuenca and J. Hesselbarth, "Self-aligned microstrip-fed spherical dielectric resonator antenna," in *Proc. 9th Europ. Conf. Antennas Propag. (EuCAP)*, Lisbon, Portugal, Apr. 2015, pp. 1–5.

[17] P. Stärke, D. Fritsche, S. Schumann, C. Carta, and F. Ellinger, "High-efficiency wideband 3-D on-chip antennas for subterahertz applications demonstrated at 200 GHz," *IEEE Trans. THz Sci. Technol.*, vol. 7, no. 4, pp. 415–423, Jul. 2017.

[18] X.-D. Deng, Y. Li, C. Liu, W. Wu, and Y.-Z. Xiong, "340 GHz on-chip 3-D antenna with 10 dBi gain and 80% radiation efficiency," *IEEE Trans. THz Sci. Technol.*, vol. 5, no. 4, pp. 619–627, Jul. 2015.

[19] A. Dyck *et al.*, "A transmitter system-in-package at 300 GHz with an off-chip antenna and GaAs-based MMICs," *IEEE Trans. THz Sci. Technol.*, vol. 9, no. 3, pp. 335–344, May 2019.

[20] A. Shamim, K. N. Salama, E. A. Soliman, and S. Sedky, "On-chip antenna: Practical design and characterization considerations," in *Proc. 14th Int. Symp. Antenna Technol. Appl. Electromagn. Amer. Electromagn. Conf.*, Ottawa, ON, Canada, Jul. 2010, pp. 1–4.

[21] C. A. Balanis, *Antenna Theory: Analysis and Design*, 3rd ed. Hoboken, NJ, USA: Wiley, 2005.

[22] L. Lewin, "Spurious radiation from microstrip," *Proc. Inst. Electr. Eng.*, vol. 125, no. 7, pp. 633–642, Jul. 1978.

[23] J. James and A. Henderson, "High-frequency behaviour of microstrip open-circuit terminations," *IEE J. Microw. Opt. Acoust.*, vol. 3, no. 5, pp. 205–218, Sep. 1979.

[24] C. Caloz and T. Itoh, *Electromagnetic Metamaterials: Transmission Line Theory and Microwave Applications: The Engineering Approach*. Hoboken, NJ, USA: Wiley, 2006.

[25] J. Al-Eryani, H. Knapp, J. Kammerer, K. Aufinger, H. Li, and L. Maurer, "Fully integrated single-chip 305–375-GHz transceiver with on-chip antennas in SiGe BiCMOS," *IEEE Trans. THz Sci. Technol.*, vol. 8, no. 3, pp. 329–339, May 2018.

[26] P. Benedek and P. Silvester, "Equivalent capacitances for microstrip gaps and steps," *IEEE Trans. Microw. Theory Techn.*, vol. MTT-20, no. 11, pp. 729–733, Nov. 1972.

[27] M. Maeda, "An analysis of gap in microstrip transmission lines," *IEEE Trans. Microw. Theory Techn.*, vol. MTT-20, no. 6, pp. 390–396, Jun. 1972.

[28] R. W. Jackson and D. M. Pozar, "Full-wave analysis of microstrip open-end and gap discontinuities," *IEEE Trans. Microw. Theory Techn.*, vol. MTT-33, no. 10, pp. 1036–1042, Oct. 1985.

[29] E. O. Hammerstad, "Equations for microstrip circuit design," in *Proc. 5th Eur. Microw. Conf.*, Hamburg, Germany, Oct. 1975, pp. 268–272.

[30] H. A. Wheeler, "Transmission-line properties of parallel wide strips by a conformal-mapping approximation," *IEEE Trans. Microw. Theory Techn.*, vol. MTT-12, no. 3, pp. 280–289, May 1964.

[31] H. A. Wheeler, "Transmission-line properties of parallel strips separated by a dielectric sheet," *IEEE Trans. Microw. Theory Techn.*, vol. MTT-13, no. 2, pp. 172–185, Mar. 1965.

[32] R. Owens, "Accurate analytical determination of quasi-static microstrip line parameters," *Radio Electr. Eng.*, vol. 46, no. 7, pp. 360–364, Jul. 1976.

[33] D. M. Pozar, *Microwave Engineering*, 4th ed. Hoboken, NJ, USA: Wiley, 2012.

[34] H. Wheeler, "Formulas for the skin effect," *Proc. IRE*, vol. 30, no. 9, pp. 412–424, Sep. 1942.

[35] D. E. Goldberg, *Genetic Algorithms in Search, Optimization, and Machine Learning*. Reading, MA, USA: Addison-Wesley, 1989.

[36] L. Lewin, "Radiation from discontinuities in strip-line," *Proc. IEE*, vol. 107, no. 12, pp. 163–170, Sep. 1960.

[37] H. Sobal, "Radiation conductance of open-circuit microstrip (correspondence)," *IEEE Trans. Microw. Theory Techn.*, vol. MTT-19, no. 11, pp. 885–887, Nov. 1971.

[38] R. E. Collin, *Antennas and Radiowave Propagation* (McGraw-Hill Series in Electrical Engineering), 1st ed. New York, NY, USA: McGraw-Hill, 1985.

[39] B. Sievert, J. T. Svejda, D. Erni, and A. Rennings, "Spherical mm-Wave/THz antenna measurement system," *IEEE Access*, vol. 8, pp. 89680–89691, 2020.

[40] T. Zwick, C. Baks, U. Pfeiffer, D. Liu, and B. Gaucher, "Probe based MMW antenna measurement setup," in *Proc. IEEE Antennas Propag. Soc. Symp.*, vol. 1, Jun. 2004, pp. 747–750.

Benedikt Sievert (Member, IEEE) was born in Krefeld, Germany. He received the B.Sc. and M.Sc. degrees in electrical engineering/high-frequency systems from the University of Duisburg-Essen, Duisburg, Germany, in 2017 and 2019, respectively.

Since 2017, he has been a member of the Laboratory of General and Theoretical Electrical Engineering, University of Duisburg-Essen. His research interests include mm-wave on-chip antennas, electromagnetic metamaterials, and theoretical and computational electromagnetics.

Jan Taro Svejda (Member, IEEE) received the B.Sc. degree in electrical engineering from the University of Applied Sciences Düsseldorf, Düsseldorf, Germany, in 2008, and the M.Sc. and Dr.Ing. degrees in electrical engineering and information technology from the University of Duisburg-Essen, Duisburg, Germany, in 2013 and 2019, respectively, with a focus on X-nuclei-based magnetic resonance imaging.

He is currently a Research Assistant with the Department of General and Theoretical Electrical Engineering, University of Duisburg-Essen, where he is involved in teaching several lectures and courses mainly in the field of electrical engineering. His general research interests include all aspects of theoretical and applied electromagnetics. He is currently focusing on medical applications, electromagnetic metamaterials, and scientific computing methods.

Jonathan Wittemeier was born in Lünen, Germany. He received the B.Sc. and M.Sc. degrees in electrical engineering and information technology from TU Dortmund University, Dortmund, Germany, in 2014 and 2016, respectively.

From 2016 to 2017, he worked in the automotive industry as a software developer. Since 2017, he has been a Research Assistant with the Institute of Integrated Systems, Ruhr University Bochum, Bochum, Germany. His current research interests are mm-wave radar, monolithic microwave integrated circuit (MMIC) design using silicon–germanium, and MIMO algorithms.

Nils Pohl (Senior Member, IEEE) received the Dipl.Ing. and Dr.Ing. degrees in electrical engineering from Ruhr University Bochum, Bochum, Germany, in 2005 and 2010, respectively.

From 2006 to 2011, he was a Research Assistant with Ruhr University Bochum, where he was involved in integrated circuits for millimeter-wave (mm-wave) radar applications. In 2011, he became an Assistant Professor at Ruhr University Bochum. In 2013, he became the Head of the Department of mm-wave Radar and High Frequency Sensors, Fraunhofer Institute for High Frequency Physics and Radar Techniques, Wachtberg, Germany. In 2016, he became a Full Professor of integrated systems with Ruhr University Bochum. He has authored or coauthored more than 100 scientific articles and has issued several patents. His current research interests include ultrawideband mm-wave radar, design, and optimization of mm-wave integrated SiGe circuits and system concepts with frequencies up to 300 GHz and above, as well as frequency synthesis and antennas.

Prof. Pohl is also a member of the Verband der Elektrotechnik Elektronik Informationstechnik e.V. (VDE), Informationstechnische Gesellschaft (ITG), European Microwave Association (EUMA), and Union Radio-Scientifique Internationale (URSI). He was a co-recipient of the 2009 EEEfCom Innovation Award, the 2012 EuMIC Prize, and the 2015 Best Demo Award of the IEEE Radio Wireless Week and a recipient of the Karl-Arnold Award of the North Rhine-Westphalian Academy of Sciences, Humanities and the Arts in 2013 and the IEEE MTT Outstanding Young Engineer Award in 2018.

Daniel Erni (Member, IEEE) received the Diploma degree in electrical engineering from the University of Applied Sciences Rapperswil (HSR), Rapperswil-Jona, Switzerland, in 1986, and the Diploma degree in electrical engineering and the Ph.D. degree in laser physics from ETH Zürich, Zürich, Switzerland, in 1990 and 1996, respectively.

Since 1990, he has been with the Laboratory for Electromagnetic Fields and Microwave Electronics, ETH Zürich. From 1995 to 2006, he was the Founder and the Head of the Communication Photonics Group, ETH Zürich. Since October 2006, he has been a Full Professor with the Department of General and Theoretical Electrical Engineering, University of Duisburg-Essen, Duisburg, Germany. He is also a Co-Founder of the spin-off company airCode, Hamm, Germany, working on flexible printed RFID technology. His current research interests include optical interconnects, nanophotonics, plasmonics, advanced solar cell concepts, optical and electromagnetic metamaterials, RF, mm-wave and THz engineering, biomedical engineering, bioelectromagnetics, marine electromagnetics, computational electromagnetics, multiscale and multiphysics modeling, numerical structural optimization, and science and technology studies (STS).

Dr. Erni is also a Fellow of the Electromagnetics Academy and a member of the Center for Nanointegration Duisburg-Essen (CeNIDE), the Swiss Physical Society (SPS), the German Physical Society (DPG), and the Optical Society of America (OSA).

Andreas Rennings (Member, IEEE) studied electrical engineering at the University of Duisburg-Essen, Duisburg, Germany. He received the Dipl.Ing. and Dr.Ing. degrees from the University of Duisburg-Essen in 2000 and 2008, respectively.

He carried out his diploma work during a stay at the University of California in Los Angeles, Los Angeles, CA, USA. From 2006 to 2008, he was with IMST GmbH, Kamp-Lintfort, Germany, where he was an RF Engineer. Since then, he has been a Senior Scientist and a Principal Investigator with the Laboratory of General and Theoretical Electrical Engineering, University of Duisburg-Essen. His general research interests include all aspects of theoretical and applied electromagnetics. He is currently focusing on medical applications and on-chip millimeter-wave/THz antennas.

Dr. Rennings received several awards, including the Student Paper Price at the 2005 IEEE Antennas and Propagation Society International Symposium and the VDE-Promotionspreis 2009 for the dissertation.